New Journal of Physics
The open access journal at the forefront of physics

Deutsche Physikalische Gesellschaft DPG IOP Institute of Physics

PAPER • OPEN ACCESS

A neural network for prediction of high intensity resonance modes in magnetic multilayers

To cite this article: A F Franco 2021 *New J. Phys.* **23** 073021

New Journal of Physics
The open access journal at the forefront of physics

Deutsche Physikalische Gesellschaft DPG
IOP Institute of Physics

Published in partnership with: Deutsche Physikalische Gesellschaft and the Institute of Physics

OPEN ACCESS

RECEIVED
7 April 2021

REVISED
9 June 2021

ACCEPTED FOR PUBLICATION
25 June 2021

PUBLISHED
13 July 2021

PAPER

A neural network for prediction of high intensity resonance modes in magnetic multilayers

A F Franco*

Centro de Investigación DAiTA Lab, Facultad de Estudios Interdisciplinarios, Universidad Mayor, Chile
* Author to whom any correspondence should be addressed.

E-mail: andres.franco@umayor.cl

Keywords: magnetic multilayers, neural networks, machine learning, ferromagnetic resonance, microwave frequency, multiband frequency device, resonance intensity

Supplementary material for this article is available online

Abstract

The use of magnetic materials as building blocks for frequency applications makes it possible to fabricate micrometer and nanometer high frequency devices. Moreover, devices with multiple high intensity modes for multiband devices can be designed by using magnetic multilayers. However, as the number of layers increases the multilayer becomes more complex, making it very difficult to find optimal configurations due to a big number of possible configurations. Fortunately, over the past decade a surge in the applicability and accessibility of machine learning algorithms and neural networks has been observed, which allow to analyse big quantities of data in search of complex patterns not always evident to humans. In this work, a theoretical model is used to generate approximately 10×10^6 data points, which in turn are used to train a neural network to calculate the number of high intensity resonance modes of three ferromagnetically coupled magnetic layers with an accuracy of over 99.8%. The neural network is then used to identify a configuration of the multilayer which provides the maximum number of high-intensity modes, and comparisons with the theoretical model are presented. Finally, the correlations between parameter were calculated over 600 million of data points, and clear guidelines for obtention of two high intensity resonance modes were identified. These results provide a simple way to find a configuration of the trilayer that have a high number of high intensity modes, thus greatly simplifying the design process of magnetic multi-band frequency devices.

1. Introduction

The use of magnetic materials as building blocks for high frequency applications makes it possible to fabricate micrometer and nanometer devices such as circulators [1, 2], phase shifters [3, 4], filters [5, 6], and frequency sources [7–12] by taking advantage of their natural resonance in the order of GHz [13, 14], making them of interest for applications in areas such as medicine [15–17], microfluidics [18–20], flexible [21–23] and printable electronics [24], magnonic devices [25], and energy harvesting [26–28].

An important requirement for the magnetic materials used for high frequency applications applications is a high magnetization, which ensures natural resonance modes with high frequency and intensity [29–32]. Exchange coupled multilayers may also fulfill these requirements. For example, in a ferromagnetically coupled bilayer (in which the magnetization of the layers tend to align parallel to each other) two resonance modes with distinguishable frequencies are observed: the low frequency acoustic (both layers are in phase) and the high frequency optical (both layers are in anti-phase) modes [33, 34]. The acoustic mode has an enhanced intensity due to the additive contribution of each layer to the frequency signal, and the optical mode has higher frequency but it is difficult to use in the practice due to its low intensity [35–39]. Using antiferromagnetic exchange coupling (which tends to align the magnetization of the layers anti-parallel to each other) enhances greatly the intensity of the high frequency mode, while reducing that of the low

frequency one [40, 41], providing a higher working frequency for applications, sacrificing access to the lower frequency mode. This illustrates that currently it is difficult to obtain multiple high intensity resonance modes using magnetic bilayers due to the intrinsic behavior of the magnetization of these structures. Another option is the use of more than two magnetic thin films, which would allow for more flexibility on their design at the cost of more complexity.

Indeed, in a previous work [42] a multilayer structure which provides multiple high frequency and high intensity resonance modes has been proposed, which could potentially be used in multiband high frequency magnetic devices. This structure is only one of the many configurations that could potentially provide multiple high intensity resonance modes. However, as the number of layers increases, the behavior of the multilayer becomes more complex and the number of combinations of physical parameters increases exponentially, making it extremely difficult to find optimal configurations. Fortunately, over the past decade a surge in the applicability and accessibility of machine learning (ML) algorithms has been observed, which allow to analyse big quantities of data in search of complex patterns not always evident to humans. These algorithms have been used for analysis of big quantities of data in industrial and scientific applications such as physics [43, 44], agriculture [45], medicine [46], and chemistry [47], allowing to analyse available data to find hidden patterns and/or predict new data when a human would have difficulty in doing so. In magnetic applications, ML has been used to analyse nucleation fields in permanent magnets [48], to study minima and magnetization switching in thin films and nanoparticles [49, 50], to estimate physical parameters from magnetic domain images [51], and to obtain effective spin Hamiltonians in magnetic systems [52]. By using ML algorithms to calculate the intensities of ferromagnetic resonance (FMR) modes, it is possible to optimize the magnetic parameters of multilayer structures that lead to a high number of high intensity resonance modes.

Neural networks are a particular kind of ML algorithms that are composed of several mathematical entities called neurons which are interconnected between them. This arrangement has allowed to analyse and predict data with more accuracy than standard ML algorithms, although with a higher computational cost for training. They have been used in a wide array of topics in medicine [53–55], biology [56–58], physics [59–61], art [62, 63], and many other areas of knowledge. In magnetism, some examples of applications include ultrafast quantum magnetism [64], frustrated magnetism [65], and calculation of hysteresis loops [66].

In this work, a neural network is trained to calculate the number of high intensity resonance modes of three ferromagnetically coupled magnetic layers as function of their physical parameters, and use the resulting model to identify multilayer configurations that have two high intensity resonant modes. In section 2 a description of the studied multilayer and the theoretical model used to generate the training data are given. In section 3 a brief description of the neural network and the training process are provided. Additionally, the process used for finding an appropriate configuration is explained. In section 4 the results obtained with the neural network under different conditions are presented, and a comparison with analytical results are shown to study its accuracy. Finally, in section 5 the correlations between the parameters have been studied for configurations with two high intensity modes, and clear tendencies have been identified.

2. System and analytical model

A scheme of the studied multilayer system is shown in figure 1. The multilayer is composed of three separate magnetic materials, which will provide three FMR modes. The gray slabs represent non-magnetic separators introduced to control the interlayer exchange coupling between magnetic films. Figure 1 also shows the reference frames used in the calculations. The reference frame defined by the layers (labeled by upper case X, Y, Z) where the XY plane represents the plane of the layer, and the magnetization reference frame (labeled by lower case x_i, y_i, z_i) where the z_i axis is along the equilibrium direction of the magnetization of the layer i and the y_i axis lies on the XY plane forming an angle φ_i with the Y axis. The x_i axis is perpendicular to both the y_i and z_i axes following a standard right hand rule. Note that depending on the equilibrium direction of the magnetization, each layer i has a set of coordinates x_i, y_i, z_i. Moreover, the angles θ and φ represent the polar and azimuthal angles in the XYZ reference frame, respectively.

For each layer i, the magnetization is given by $\vec{M}_i(\vec{r};t) = M_i^{(0)}\vec{e}_{z_i} + m_{x_i}(\vec{r};t)\,\vec{e}_{x_i} + m_{y_i}(\vec{r};t)\,\vec{e}_{y_i}$, where $M_i^{(0)}$ is a static uniform component of the magnetization and m_{x_i} and m_{y_i} are dynamical components. Assuming that the later two are very small (linear regime), the approximation $M_i^{(0)} \approx M_i - \frac{1}{2M_i}[(m_{x_i})^2 + (m_{y_i})^2]$ is performed, where M_i is the saturation of the layer i. This approximation is then introduced in the Hamiltonian $\mathcal{H}$ of each contribution [e.g. $\mathcal{H} = \mu_0 \int_V \vec{H} \cdot \vec{M}_i(\vec{r};t)\,\mathrm{d}\vec{r}$ for the Zeeman contribution, where $\vec{H}$ is the external applied field]. Afterwards, the dynamical components are written in

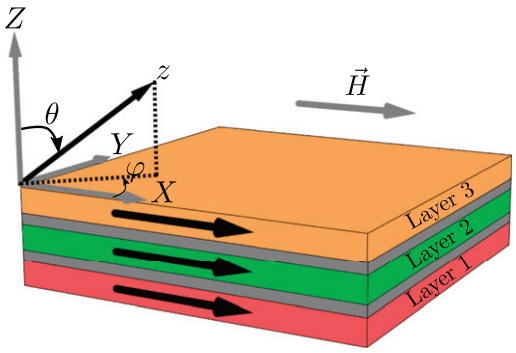

Figure 1. Scheme of the multilayer. Grey slabs represent non-magnetic separators introduced to control the interlayer exchange coupling between magnetic films. Two rectangular reference frames are defined. Uppercase X, Y, Z use the plane of the layer as reference, and lowercase x, y, z use direction of the magnetization ($z\|\vec{M}$, y on the XY plane).

the k-space through the Fourier transform as [67–69] $m_{\alpha_i}(\vec{r};t) = \frac{1}{\sqrt{L^2 d}}\sum_{\vec{k}_i} m_{\alpha_i}\left(\vec{k}_i\right)\exp\left[\mathrm{i}\left(\vec{k}_i\cdot\vec{r}-\omega t\right)\right]$, and the Hamiltonian takes the form

$$\mathcal{H} = \mu_0 \sum_{\vec{k}_\parallel} \sum_{i=1}^{n}\sum_{j=i}^{n}\sum_{\alpha,\beta=x,y} \frac{H_{\alpha_i\beta_j}}{2M_i}\left(\vec{m^{k}_{\alpha_i}}\right)^{*}\vec{m^{k}_{\beta_j}}, \tag{1}$$

after taking only the second order contributions of m_{x_i} and m_{y_i}. Here, $m^{\vec{k}}_{\alpha_i} \equiv m_{\alpha_i}\left(\vec{k}_i\right)$, and the fields $H_{\alpha_i\beta_j}$ are dynamical fields with expressions that depend on the specific contribution and on the equilibrium direction of the magnetization.

The time evolution of the magnetization is given by the Heisenberg equation of motion $\mathrm{i}\hbar\dot{m}^{\vec{k}}_{\alpha_i} = \left[m^{\vec{k}}_{\alpha_i}, \mathcal{H}\right]$, where $\alpha = x, y$. Inserting (1) into this equation of motion, the following expressions are obtained

$$\begin{aligned}
\mathrm{i}\hbar\dot{m}^{\vec{k}}_{x_i} &= -\mathrm{i}\mu_i \sum_{\zeta=i-1}^{i+1} \mu_0\left(H_{y_i x_\zeta} m^{\vec{k}}_{x_\zeta} + H_{y_i y_\zeta} m^{\vec{k}}_{y_\zeta}\right)\\
\mathrm{i}\hbar\dot{m}^{\vec{k}}_{y_i} &= \mathrm{i}\mu_i \sum_{\zeta=i-1}^{i+1} \mu_0\left(H_{x_i x_\zeta} m^{\vec{k}}_{x_\zeta} + H_{x_i y_\zeta} m^{\vec{k}}_{y_\zeta}\right),
\end{aligned} \tag{2}$$

where the properties of commutation that read $[A, BC] = [A, B]C + B[A, C]$, $[A, B] = -[B, A]$ have been used, along the commutation rules $[m_{x_i}(\vec{k}), m_{y_i}(-\vec{k})] = \mathrm{i}\mu_i M_s^i \delta_{\vec{k}_\parallel,\vec{k}_\parallel}$ and $[m_{y_i}(\vec{k}), m_{x_i}(-\vec{k})] = -\mathrm{i}\mu^i M_s^i \delta_{\vec{k}_\parallel,\vec{k}_\parallel}$. Here, μ_i is the magnetization of the unit cell of the layer i. By writing (2) for all i in matricial form, we obtain

$$\begin{bmatrix} \dot{m}^{\vec{k}}_{x_0} \\ \dot{m}^{\vec{k}}_{y_0} \\ \vdots \\ \dot{m}^{\vec{k}}_{x_{n-1}} \\ \dot{m}^{\vec{k}}_{y_{n-1}} \end{bmatrix} = -\gamma D_{\mathrm{m}} \begin{bmatrix} m^{\vec{k}}_{x_0} \\ m^{\vec{k}}_{y_0} \\ \vdots \\ m^{\vec{k}}_{x_{n-1}} \\ m^{\vec{k}}_{y_{n-1}} \end{bmatrix}, \tag{3}$$

where $\gamma = -\mu_i/\hbar = 1.76\times 10^{11}\ \mathrm{T\ s^{-1}}$ is the gyromagnetic ratio, and D_{m} is the dynamical matrix given by [37]

$$D_{\mathrm{m}} = \mu_0\gamma \begin{bmatrix} -H_{y_1x_1} & -H_{y_1y_1} & -H_{y_1x_2} & -H_{y_1y_2} & \dots \\ H_{x_1x_1} & -H_{x_1y_1} & H_{x_1x_2} & -H_{x_1y_2} & \dots \\ -H_{y_2x_1} & -H_{y_2y_1} & -H_{y_2x_2} & -H_{y_2y_2} & \dots \\ H_{x_2x_1} & -H_{x_2x_1} & H_{x_2x_2} & -H_{x_2y_2} & \dots \\ \vdots & \vdots & \vdots & \vdots & \ddots \end{bmatrix}. \tag{4}$$

Moreover, (3) can also be written as $\dot{\vec{m}} = -\gamma D_{\mathrm{m}}\vec{m}$, where $\vec{m}$ and $\dot{\vec{m}}$ are vectors containing the dynamical components of the magnetizations of all layers and their time derivative, respectively. Using the components in the k-space, the time derivative can be written as $\dot{\vec{m}} = -\mathrm{i}\omega\vec{m}$, which allows to rewrite (3) as

$(D_{\rm m} + {\rm i}\omega I)\,\vec{m} = 0$, with I being the identity matrix. The resonance frequencies of the system are obtained after solving this equation, and thus are given by the negative eigenvalues of the matrix $D_{\rm m}$. For each individual layer i, the dynamical fields $H_{\alpha_i\beta_i}$ account for the contributions from the external magnetic field $\vec{H}$ and the demagnetizing field. They are given by [67–69]

$$H^I_{x_ix_i} = H + M_i \qquad H^I_{y_iy_i} = H, \tag{5}$$

where the magnetization of all layers and $\vec{H}$ are assumed to be along the X axis. Expressions that relax these constraints can be found in [37, 42].

Additionally, the interlayer exchange coupling contributions to the dynamical fields are given by

$$\begin{aligned} H^J_{x_ix_i} &= H^J_{y_iy_i} = \sum_j \frac{J^{ij}_{\rm eff}}{\mu_0 M_i t_i} \\ H^J_{x_ix_j} &= H^J_{y_iy_j} = -\frac{J^{ij}_{\rm eff}}{\mu_0 M_j t_i} \\ H^J_{x_iy_j} &= H^J_{y_ix_j} = 0. \end{aligned} \tag{6}$$

The summation over j refers to the neighboring layers $i+1$ and $i-1$, and t_i is the thickness of the layer i. $J^{ij}_{\rm eff}$ is the effective exchange coupling constant between layers i and j, and is positive for ferromagnetic coupling and negative for antiferromagnetic exchange. The fields composing the matrix (4) are then given by $H_{\alpha_i\beta_j} = H^I_{\alpha_i\beta_j} + H^J_{\alpha_i\beta_j}$. Finally, for thin films with uniform magnetization and lateral dimensions much larger than their thickness the dipolar coupling contribution to the FMR is negligible [42, 70, 71].

The magnetic susceptibility $\chi_{\alpha\beta}$ provides information on the intensity of oscillation of the different resonance modes, and in the linear regime is defined as $m_\alpha = \chi_{\alpha\beta} h_\beta$. It provides the response of the α component of the dynamical magnetization to a small dynamical field h_β applied in the β direction. It is obtained from the components of the susceptibility tensor

$$\chi \equiv \begin{bmatrix} \chi^{1,1}_{xx} & \chi^{1,1}_{xy} & \chi^{1,2}_{xx} & \chi^{1,2}_{xy} & \cdots \\ \chi^{1,1}_{yx} & \chi^{1,1}_{yy} & \chi^{1,2}_{yx} & \chi^{1,2}_{yy} & \cdots \\ \chi^{2,1}_{xx} & \chi^{2,1}_{xy} & \chi^{2,2}_{xx} & \chi^{2,2}_{xy} & \cdots \\ \chi^{2,1}_{yx} & \chi^{2,1}_{yy} & \chi^{2,2}_{yx} & \chi^{2,2}_{yy} & \cdots \\ \vdots & \vdots & \vdots & \vdots & \ddots \end{bmatrix}, \tag{7}$$

where $\chi^{i,j}_{\alpha\beta}$ is the response of the α component of the dynamical magnetization of the layer i to a small dynamical field applied in the β direction to the layer j. The total susceptibility is obtained by summing over the different combinations of α, β, i and j, and accounting for the orientation of the magnetization of each individual layer. Assuming all the magnetic moments lie on the XZ plane, it is calculated using

$$\chi_{yy} = \sum_i \sum_\eta \frac{t_i}{t_{\rm T}} \chi_{y_iy_\eta}, \tag{8}$$

where $t_{\rm T}$ is the sum of the thicknesses of all the magnetic materials.

The susceptibility tensor (7) can be obtained by using $\chi = D_{\rm g}^{-1} M_{\rm T}$, where

$$M_{\rm T} \equiv \begin{bmatrix} 0 & -M_1 & 0 & 0 & \ldots \\ M_1 & 0 & 0 & 0 & \ldots \\ 0 & 0 & 0 & -M_2 & \ldots \\ 0 & 0 & M_2 & 0 & \ldots \\ \vdots & \vdots & \vdots & \vdots & \ddots \end{bmatrix}, \tag{9}$$

and $D_{\rm g} = {\rm i}\frac{\omega}{\gamma} W + D_{\rm m}$. ω is the angular frequency of the microwave field, and the matrix W is given by

$$W = \begin{bmatrix} 1 & g_1 & 0 & 0 & \ldots \\ -g_1 & 1 & 0 & 0 & \ldots \\ 0 & 0 & 1 & g_2 & \ldots \\ 0 & 0 & -g_2 & 1 & \ldots \\ \vdots & \vdots & \vdots & \vdots & \ddots \end{bmatrix}, \tag{10}$$

with g_i being the Gilbert damping parameter of the layer i.

3. Training data and neural network

Using (8), the susceptibility for several combinations of physical parameters of the multilayer is calculated. A fixed ferromagnetic exchange coupling $J_{\text{eff}}^{ij} = 0.15$ mJ m^{-2} is used, and an in-plane external magnetic field $\mu_0 H = 0.1$ T is applied along the X axis. Thus the multilayer is always saturated along the field. The thickness is varied between $t = 1$ nm and $t = 5$ nm, and the saturation is varied between $M_i = 500$ kA m^{-1} and $M_i = 950$ kA m^{-1}. From the experimental point of view, control of the saturation can be achieved by adding non-magnetic materials to standard magnetic alloys, e.g. by using different Cu ratios in NiFeCu thin films [36]. For each combination of parameters, the number of high intensity resonant peaks were calculated. In each case, the resonant mode with highest intensity was identified, and then all resonant modes with at least 20% intensity (when compared to the highest intensity) were taken into account.

When generating the training data, the number of calculated data point scales with $(n_t n_M)^3$, where n_t and n_M are the number of values taken for the thickness and saturation of each layer, respectively. This means that with $n_t = 10$ and $n_M = 10$, a total of 10^6 points would be calculated. Using these rules, six data sets were generated: two with equally spaced values ($n_t = 10$, $n_M = 10$ and $n_t = 13$, $n_M = 13$), and four with randomly distributed parameters (all with 10^6 points). The six data sets were then combined into a single data set with almost 10×10^6 data points to be used as training data for the neural network.

A multi-layer perceptron (MLP) neural network classifier from Python's scikit-learn library [72] was used. Standard classifier algorithms are based on a linear combination of nonlinear basis functions $\phi_i(\mathbf{D})$ that take the form

$$O(\mathbf{D}, \mathbf{W}) = f\left(\sum_{i=i}^{m} w_i \phi_i(\mathbf{D})\right), \tag{11}$$

where $f(x)$ and $\phi(x)$ are nonlinear functions. $\mathbf{D}$ is the input data, $\mathbf{W}$ are the weights w_i assigned to the functions $\phi_i(\mathbf{D})$, and m is the number of basis functions used. For neural networks, the basis functions $\phi_i(\mathbf{D})$ themselves also take the form given by (11) [73], and each level of depth is known as a layer. Knowing that each function $\phi_i(\mathbf{D})$ represents a neuron, an interconnected system is obtained where the results provided by a given neuron depends on the results obtained by previous neurons in the network. In MLP, each layer behaves similar to a single perceptron classifier [73] that uses a logistic sigmoid or a softmax function for $f(x)$ and $\phi(x)$ instead of a step-function. The training process then involves finding the appropriate weights $\mathbf{W}$ of each neuron that allow to minimize the total error of the prediction. In this particular case, a two level MLP (one main layer and one hidden layer) with 100 neurons each is used ($m = 100$). The activation functions $f(x)$ and $\phi(x)$ are given by the rectified linear unit function $f(x) = \max(0, x)$, and the learning process is performed using the Adam algorithm proposed by Kingma and Ba [74].

Training and testing was performed using a stratified 80%–20% split of the normalized data set. A standard minimum–maximum normalization was used, and the normalization rules were saved in an independent file to be used when predicting new data. Moreover, the data sets are highly unbalanced (99% of the data produces only a single high intensity peak), which has to be accounted for before training the neural network. This was done by combining standard under-sampling of the majority class (randomly deleting data with single peaks) alongside synthetic minority over-sampling technique [75] for simulating new data of the minority class (data with two or more peaks). To generate the new data, the k-nearest neighbors to a data point of the minority class are identified, and then k new points are generated, each in the direction of a nearest neighbor.

After the preprocessing, the MLP was trained and the resulting confusion matrix is shown in table 1. An accuracy of more than 99.8% is obtained for both the majority (1 peak) and the minority (2 peaks) classes. However, due to the imbalance of the data, even a very low percentage of misclassified majority class will lead to an important percentage of false positives of the minority class. In this case this percentage reaches $\approx 16.4\%$. Note that all the data sets, the trained model, the normalization rules, the python codes used for training the neural network, and a python code for predicting the number of peaks of a single combination of parameters are available as supplementary material (https://stacks.iop.org/NJP/23/073021/mmedia). Moreover, note that with three magnetic layers, three resonance peaks are expected. However, throughout all the training data there was not a single instance of a third high intensity mode, and thus it was not accounted for in the training of the MLP.

The final step is to identify a combination of parameters which provides a 2-peaked response function. As starting point, a data point with 2 peaks was selected from the training data. Although not necessary, this step greatly simplifies the search as only $\approx 1\%$ of the total space of parameters lead to a response function with 2 high intensity peaks. However this is not enough, as it is necessary to adjust the multilayer configuration to be as close as possible to the available materials and to be stable under experimental

Table 1. Confusion matrix comparing the training data with the results obtained from the trained MLP neural network.

	1 peak (predicted)	2 peaks (predicted)
1 peak (theory)	791 555	1383
2 peaks (theory)	6	7056

Table 2. Physical parameters of the multilayer system. Parameters with (*) have been identified through the ML model for maximization of the number of high intensity resonant modes.

	t_i^* (nm)	M_i^* (kA m^{-1})	$\mu_0 H$ (T)	J_{eff}^{ij} (mJ m^{-2})
Layer 1	4.5	510		
Layer 2	2	800	0.1 along X	0.15
Layer 3	4.5	900		

variations. Thus, individual parameters were varied and the number of peaks were studied using the MLP, and stable values (far away from transitions) were chosen arriving to the configuration shown in table 2.

4. Results and discussion

In this section, results obtained through the ML model are shown, and comparisons with the results given by the analytical model (8) are presented. Table 2 shows the physical parameters of the multilayer used for all the results presented in this section. Note that t_i and M_i were identified using the trained ML model, and an * has been added to their names to clarify this. The interlayer exchange coupling is given between neighboring layers. All of these parameters can be tuned from the experimental point of view. For example, M_i can be varied during the fabrication process by adjusting the ratio of non-magnetic vs magnetic materials in an alloy [36], and J_{eff}^{ij} can be adjusted through the thickness of the non-magnetic separator between layers i and j [76–78]. All the results of this section use these parameters unless specified otherwise.

Figure 2 shows the response function of the multilayer, as given by (8). In all cases, two high intensity resonance modes can be observed. Figure 2(a) shows the effect of the in-plane applied field. Here, it can be observed that as the field increases, the frequencies of all modes tends to increase. This is expected as the system always remains in a saturated state due to the ferromagnetic interlayer exchange coupling. Moreover, although the intensity of the low frequency mode decreases with an increasing field, the intensity of the high frequency mode remains mostly constant. This is a very interesting result, as typically the intensity of the resonance modes in magnetic thin films and multilayers tends to decrease as the frequency increases.

Another apparent deviation from expected results is the existence of only two resonance modes, as normally there should exist one mode for each magnetic layer within the structure [33, 37, 40, 42]. Indeed, in all cases the theoretical calculations show the existence of three resonance modes. However, the third mode (with the highest frequency) has a very weak intensity in all the observed parameter space. This is related to the decrease of intensity typically observed for high frequency modes, combined with the relative contribution of the layers to each mode. Because this mode has very low intensity for all the studied space of parameters, it was not accounted for when training the ML model.

These contributions are shown in figure 2(b), where the susceptibility of each individual layer as function of the frequency is presented (for $\mu_0 H = 0.1$ T). Here it can be seen that the low frequency mode has an additive contribution from all layers, meaning that all the layers precess in phase. The second high intensity mode has additive contributions from layers 2 and 3 (they are in phase), and a subtractive contribution from layer 1. However the contribution from the layer 2 is stronger than that of the layer 1, and thus the resulting mode also has high intensity. Note that the negative susceptibility observed in the layer 1 means that the oscillations of this layer have a phase of π respect to the layers 2 and 3. The third mode (not shown due to a low intensity of all contributions) has additive contributions from layers 1 and 3, and subtractive contribution from layer 2. Here not only the contributions of each individual layer are very weak due to the high frequency, but also the subtractive contribution of the layer 2 is stronger, thus decreasing even more the total intensity of the mode.

Figure 3 shows the number of high intensity modes as function of t_i and M_i for each layer, and compares the MLP and analytical results. Dark colors represent two high intensity modes, while light colors represent one mode. Note that figure 3 shows slices of the multi-dimensional phase diagram composed by the six-dimensional hyperspace with axes M_1, M_2, M_3, t_1, t_2, t_3. It can be observed that in all cases the MLP (figures 3(a)–(c)) reproduces really well the analytical results (figures 3(d)–(f)), although there are some differences around the transition between regions. This is more evident in figures 3(b) and (e), which show

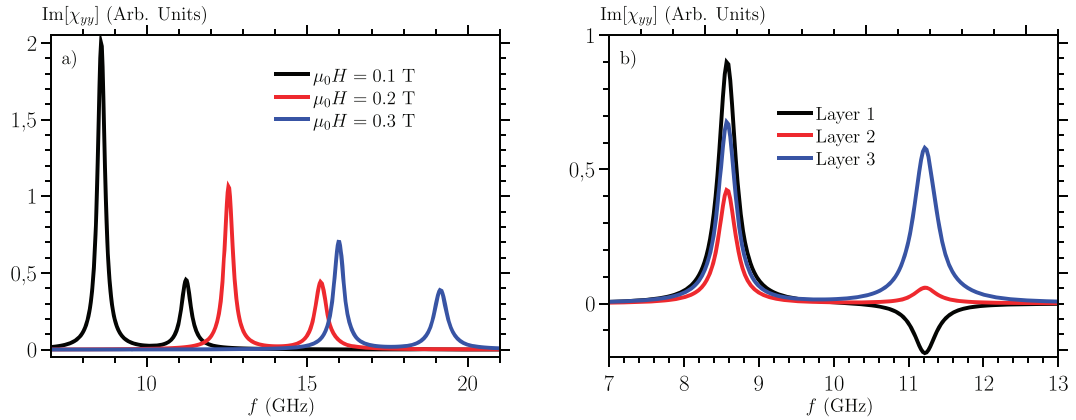

Figure 2. Susceptibility χ_{yy} as function of the frequency. (a) Effect of various values of the in-plane applied field and (b) contribution of individual layers to the resonance modes with $\mu_0 H = 0.1$ T.

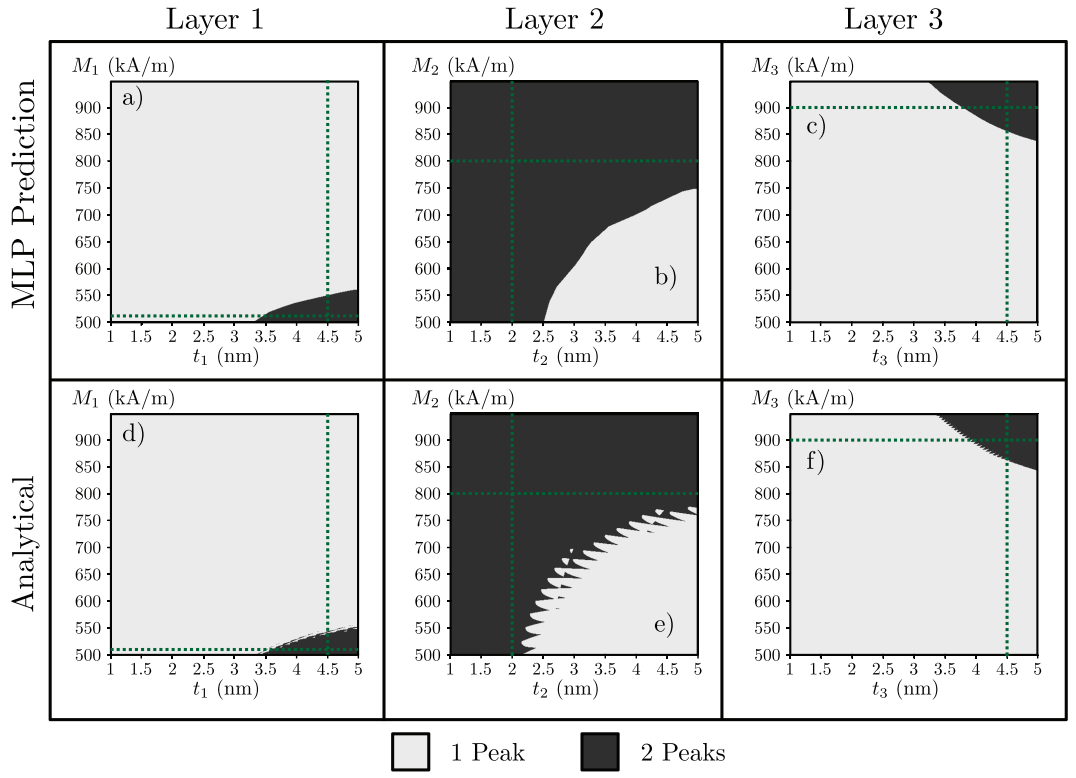

Figure 3. Number of high intensity modes as a function of t_i and M_i for the ((a) and (d)) layer 1, ((b) and (e)) layer 2, and ((c) and (f)) layer 3. Results of (a)–(c) the MLP prediction and (d)–(f) the analytical expression (8). Dashed lines represent the data shown in figure 4

the phase diagram obtained when the parameters of the layer 2 are varied. Here, the analytical model shows a rugged transition, which the MLP is not able to reproduce. This uneven transition is due to the way in which the high intensity modes are defined. As discussed previously, for each individual combination of parameters there is always at least one high intensity mode, and a second mode will be taken into account if it has an intensity of at least 20% compared to the mode with maximum intensity. Around the transition between regions, small changes in t_i and/or M_i will lead to small changes in the intensities of all resonant modes, which will constantly take the low intensity mode in and out the 20% threshold, inducing the observed ruggedness.

A more direct comparison is shown in figure 4, where the number of high intensity modes as a function of either t_i (figure 4(a)) or M_i (figure 4(b)) is presented. Solid lines represent the MLP predictions, and the dashed lines with circles represent the results given by (8). The different colors indicate which layer had its parameters varied, and the individual curves were displaced vertically for clarity. Again, a very good

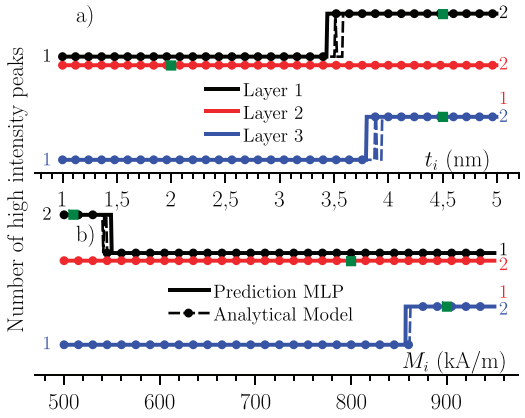

Figure 4. Number of high intensity modes as a function of (a) t_i or (b) M_i for the each layer. Comparison between the ML model (solid lines) and the analytical expression (8) (dashed line with circles). Green data points represent the data shown in table 2.

agreement between the two can be observed in all cases, with some differences present at the transition between the regions. The ruggedness is observed again, represented by a constant swapping of the analytical results between 1 and 2.

5. Parameters correlation

After training the MLP neural network and showcasing its high accuracy, it is used to analyse more in depth the trilayer system and how its magnetic parameters are related to the presence or absence of a second high intensity resonance mode. With this objective, 638 million of data points were calculated using the same range of the physical parameters as that used in the training of the neural network ($M_i = 500$–950 kA m^{-1} and $t_i = 1$–5 nm for all i). Between those ranges, M_i was divided in 41 different values with equal separation ($\Delta M = 11.25$ kA m^{-1}). Similarly, t_i was divided in 21 values with equal separation ($\Delta t = 0.2$ nm). Although the number of values that each parameter takes may appear small, the number of calculated data points increases exponentially due to the six-dimensional space in which the model is applied. This also means that a good statistic description is possible due to the high amount of data points. Finally, note that the study presented in this section was only possible by using the trained MLP neural network because it is two orders of magnitude faster than the standard analytical model (8) (the 600+ million of data points were calculated in 1 day using the neural network, while the 10 million training data were calculated in 2 days using analytical calculations).

Figure 5 shows the normalized histogram of all parameters for configurations of the trilayer which present two high intensity resonance modes, providing information of the values of the parameters for which is most probable to obtain these modes. The first behavior that can be observed is that the layers 1 and 3 have identical behavior in both M and t. This is expected as interchanging the parameters of these two layers would lead to identical results due to the symmetry of the trilayer. However, note that this does not means that layer 1 and 3 always take the same values, and the observed histogram is obtained only after taking into account all calculated data points with two peaks.

Figure 5(a) shows the histogram of M_i, where it can be observed that it is more probable to find high intensity modes when M_1 and M_3 are near the extreme values of $M_i = 500$ and 950 kA m^{-1}. On the other hand, M_2 is distributed more uniformingly, although the probability increases slowly with M_2. Figure 5(b) shows the histogram of t_i. In this case, t_1 and t_3 tend to induce two resonance modes for high values, reaching a maximum at the extreme value of 5 nm. On the other hand, t_2 is again more evenly distributed, with increasing probability as it decreases towards 1 nm. These tendencies are expected to continue beyond the limit values presented. Moreover, these tendencies are also expected to remain for other limit values of the parameters (e.g. for $M_i = 1000$–2000 kA m^{-1}, the peak values would be observed around $M_1 = M_3 = 1000$ and 2000 kA m^{-1}).

To better understand how the data shown in figure 5 is distributed throughout the different possible parameter combinations, the correlation coefficient

$$r_{xy} = \frac{\sum (x_i - \bar{x})(y_i - \bar{y})}{\sqrt{\sum (x_i - \bar{x})^2 \sum (y_i - \bar{y})^2}} \tag{12}$$

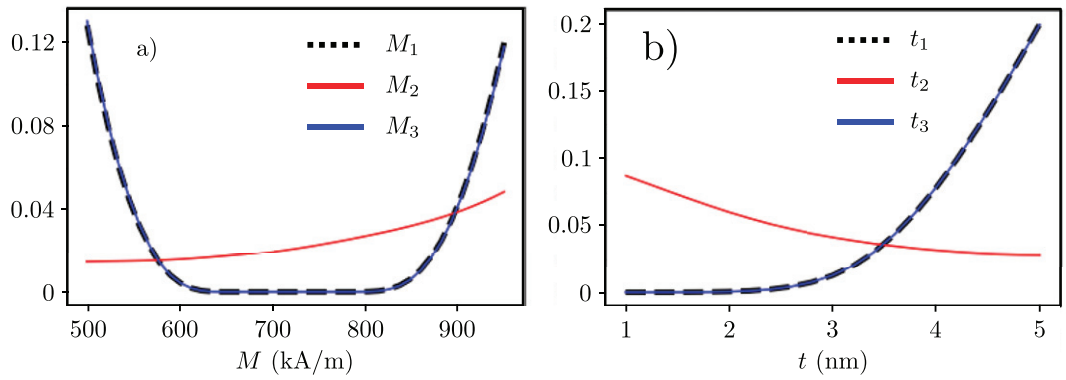

Figure 5. Histogram of (a) M_i and (b) t_i for trilayers with two high intensity resonant modes, normalized to the total number of data points with these modes. The dashed black lines, red lines, and blue lines represent, respectively, the layer 1, 2, and 3.

Table 3. Correlation matrix containing the correlation coefficients r_{xy} of all pairs of studied magnetic parameters, as given by (12). Blue values represent positive correlation, green values are negative correlation, and grey values represent very weak correlation.

	M_1	M_2	M_3	t_1	t_2	t_3
M_1	1					
M_2	-4.53×10^{-4}	1				
M_3	−0.979	-4.10×10^{-3}	1			
t_1	0.180	-5.14×10^{-3}	−0.183	1		
t_2	-4.56×10^{-3}	0.284	-6.21×10^{-3}	8.76×10^{-2}	1	
t_3	−0.191	-7.97×10^{-3}	0.188	−0.205	8.72×10^{-2}	1

is calculated for every pair of parameters, and the results are shown in table 3. Blue cells indicate a positive correlation, indicating that both parameters tend to increase or decrease at the same time. This positive correlation is present for all parameter within a single layer (M_1t_1, M_2t_2, and M_3t_3). Green cells indicate a negative correlation, which indicates that when one parameter increases, the other decreases, and is present when comparing parameters of the outside layers 1 and 3. In particular, the correlation M_1M_3 is almost -1 indicating that the relation between both saturations is very closely given by $M_1 = -M_3 + 1450$ kA m^{-1} (the value 1450 kA m^{-1} ensures that the lineal dependence is observed between 500 and 950 kA m^{-1}). However, do note that these values are concentrated around the edges of the observed space of parameters, as shown in figure 5(a). Finally, gray values indicate there is almost no correlation between the parameters, and occur for all the combinations of parameters of outside layers with the middle one, e.g. M_1t_2, M_2t_1, M_2M_3, etc.

For a better visualization of these correlations, two-dimensional histograms relating pairs of parameters are shown in figure 6. Each subfigure labeled from (a) to (o) represents a pair of parameters, following the same order presented in table 3, ignoring comparisons of the parameters with themselves (blue cells with correlation 1). For clarity of the presented information, the color scale of the figures is not shared between histograms. Nonetheless, black regions always indicate high number of data points with 2 high intensity modes, while white regions indicate that 2 high intensity modes were not obtained. This is necessary to be able to observe a detailed behavior for all pairs of parameters, e.g. figure 6(h) representing the correlation M_2t_2 would look as a clear uniform color if the color scales were shared, as the data points are distributed over a fairly wide region instead of concentrated in one or two corners of the two-dimensional space.

Figure 6(b) represents the M_1M_3 correlation. As discussed previously, these two parameters have a strong negative correlation concentrated around the edges of the observed space. This is clearly represented in the histogram, in which two black regions concentrated in opposite corners of the figure are observed. This indicates that in order to obtain two high intensity modes, M_1 would need to take values around 950 kA m^{-1} when M_3 is near 500 kA m^{-1}, and vice versa. Other pairs of parameters with negative correlation are shown in figures 6(f), (k) and (n) (correlation pairs M_3t_1, M_1t_3, and t_1t_3, respectively). In (f) and (k), two black regions are observed. One is concentrated around low values of M and high values of t, and the other one concentrated around high values of M, but spread over high-intermediate values of t. Here, the negative correlation is given mostly by the presence of the first more intense region, however the second region is necessary because, as observed in the M_1M_3 correlation (figure 6(b)), M_1 and M_3 will always take opposite values on the observed space which has a consequence that figures 6(f) and (k) cannot

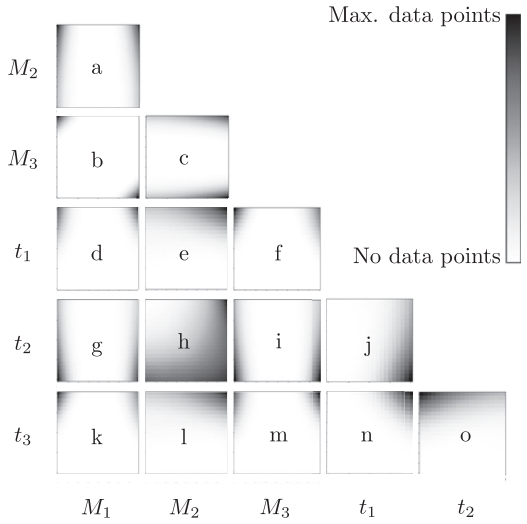

Figure 6. Two-dimensional histograms relating pairs of parameters of the trilayer system. Each figure (a)–(o) represents a different pair of parameters, using the same order shown in table 3. Black regions indicate high number of data points with 2 high intensity modes, while white regions indicate that 2 high intensity modes were not obtained. All M_i vary between 500 and 950 kA m^{-1}. All t_i vary between 1 and 5 nm.

be both in the high intensity region at the same time. Finally, figure 6(n) shows that both t_1 and t_3 are concentrated around 5 nm. In this case the negative correlation is somewhat misleading, as it represents a negative slope on the dependence between t_1 and t_3 in values concentrated around the upper-right corner of the figure.

Figures 6(d), (h) and (m) represent parameter pairs with positive correlation. Figures 6(d) and (m) correlate M_it_i of the layers 1 and 3, respectively. It can be observed that these histograms are a mirror of the ones observed in figures 6(k) and (f). This means that the layer with high M_i needs to have high t_i, while the thickness of the layer with low M_i is more evenly distributed around high-intermediate values. Figure 6(h) relates the magnetization and thickness of the middle layer, i.e. M_2t_2. This is the most evenly distributed histogram of all the figures, as it would be expected from the red curves in figure 5. However there is clear tendency towards high M and low t values.

The remaining figures in the histogram (figures 6(a), (c), (g), (e), (l), (i), (j) and (o)) represent histograms with very low correlations, and they all relate a parameter of one of the outer layers (1 or 3) with a parameter of the middle one (layer 2). In figures relating M_1 or M_3 with either M_2 or t_2 ((a), (c), (g), (i)), the former two are concentrated in either high or low values of M, while the parameters of the layer 2 are more evenly distributed (again, with a slight preference for high values of M_2 and low values of t_2). On the other hand, in figures relating t_1 or t_3 with either M_2 or t_2 ((e), (l), (j), (o)), the thicknesses of the outer layers take high values and the parameters of the layer 2 are evenly distributed.

From this analysis of correlations, the following tendencies that would lead to a second high intensity resonance mode in the trilayer were identified:

- The saturation of the outer layers need to be as separated as possible. Thus, one layer would have high saturation M_H and the other would have low saturation M_L.
- The outer layer with M_H needs a high thickness t_H. However, care should be taken to ensure that the magnetization of the layer is uniform over all the thickness of the layer.
- The thickness of the outer layer with M_L can take a wider set of values for the thickness, but again better results are obtained for high thicknesses.
- The parameters of the middle layer can take almost any value, although more stable results would be obtained with a saturation near M_H and a low thickness.

In order to test wether these tendencies hold for different values of the parameters, the limit values of M_i will be changed and the frequency response of the resulting trilayer will be calculated using the analytical model (8). The parameters of the new trilayer are $M_1 = M_2 = 2000$ kA m^{-1}, $M_3 = 1000$ kA m^{-1}, $t_1 = t_3 = 5$ nm, and $t_2 = 1$ nm. These combination of parameters fulfill with the conditions for obtaining a second high intensity mode presented just above. Moreover, note that although the values of M_i changed, the same values of t_i were taken. This is because non-uniform magnetization may arise over the thickness of the layer if it is increased beyond 5 nm, making the analytical model (8) invalid. Figure 7(a) shows the response function of the new multilayer as function of the frequency, where the presence of two high

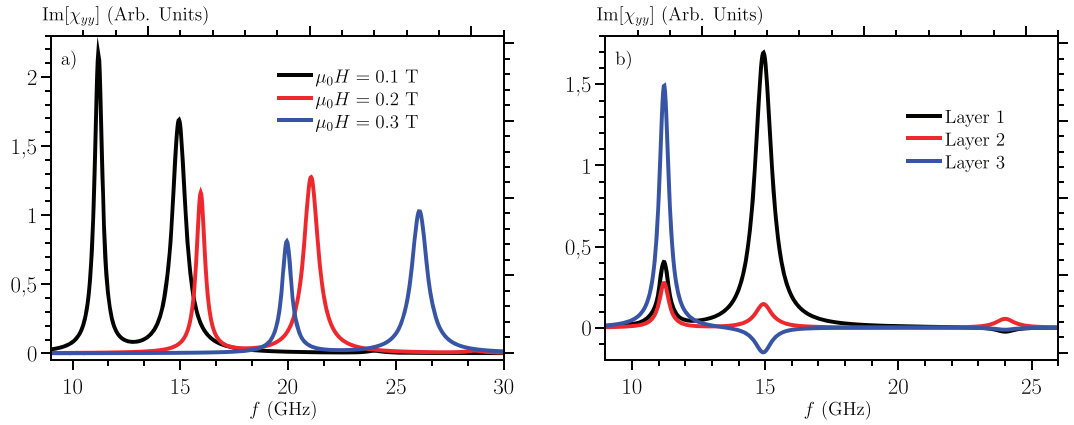

Figure 7. Susceptibility χ_{yy} as function of the frequency, using saturation values of $M = 1000$ and 2000 kA m^{-1}. (a) Effect of various values of the in-plane applied field and (b) contribution of individual layers to the resonance modes with $\mu_0 H = 0.1$ T.

intensity resonance modes can be clearly observed for several values of the applied field, with even higher intensities that those shown in figure 2(a). The contributions of individual layers to the susceptibility with $\mu_0 H = 0.1$ T are shown in figure 7(b). Very similar contributions to those shown in figure 2(b) are observed, that is, the low frequency mode has an additive contribution from all layers (all the layers precess in phase), and the second high intensity mode has additive contributions from layers 1 and 2 (they are in phase) and a subtractive contribution from layer 3 (anti-phase precession). In this case, the layer 1 has additive contribution instead of the layer 3 (which was the case for the results shown in figure 2(b)) because the former has a higher saturation.

Finally, from the results shown in figures 2(b) and 7(b), and taking into account that the intensity contributions of each layer are directly related to the $M_i t_i$ product, the following physical interpretation can be given to the obtained conditions for high intensity modes. The second intensity peak showcases additive contributions from the middle layer with the outer layer with M_H, and subtractive contribution from the remaining outer layer with M_L. Thus, by making $M_1 = M_2 = M_H$ and $M_3 = M_L$, we ensure that the additive contributions are as high as possible, while keeping the subtractive contribution low. Similarly, $t_1 = t_H$ ensures a high additive contribution of the layer 1 to the second resonance mode. Following the same logic, one would expect that $t_3 = t_L$ would decrease the subtractive contribution. However a low thickness also means a stronger interlayer exchange coupling field as they are inversely proportional (see (6)). This means that with $t_3 = t_L$, it would be more energetically favorable for the layer 2 to precess in phase with the layer 3 instead of the layer 1. Thus, there would be one strong positive contribution to the susceptibility (from layer 1) and two mid to low negative contributions (layers 2 and 3), leading to a second resonance mode with lower intensity. Making $t_1 = t_3 = t_H$ ensures that the layer 1 and 2 precess in phase. For t_2, a wide range of values are possible, but in general there are two limit behaviors: $t_2 = t_H$ would provide higher intensity modes, while $t_2 = t_L$ provides more stability under experimental variations of individual parameters. Nonetheless, after using the MLP to identify parameter combinations that provide the desired number of high intensity modes, it is recommended to perform theoretical calculations and/or micromagnetic simulations in order to ensure that the predictions are correct.

6. Conclusions

A theoretical model was used to calculate the susceptibility and number of high intensity FMR modes of a magnetic trilayer for several combinations of thicknesses and magnetic saturation of each layer. Approximately 10×10^6 data points were generated, and used to train a MLP neural network to classify the data according to the number of peaks found in the susceptibility. After taking appropriate measures such as normalization and balancing of the training data, a neural network with an accuracy of more than 99.8% was obtained.

The neural network was then used to identify a combination of parameters of the multilayer which provides the maximum number of high-intensity modes. Two high intensity modes at different frequencies are obtained which are robust under in-plane external magnetic fields. Although the intensity of low frequency mode tends to decrease as the field increases, the intensity of the high frequency mode remains constant. Moreover the frequency of both modes increases with the field because the magnetization of the layers are always aligned with it.

The parameters of the multilayer were varied to test for stability and to compare the predictions with results from the theoretical model. In all cases the neural network reproduces the theoretical data remarkably well, with some differences around transitions in the number of peaks.

Finally, correlations between the paramaters were calculated based on 600+ million of data points obtained by using the trained ML model. After analysing these correlations, basic guidelines that ensure two high intensity resonant modes were identified, and physical interpretations of why these particular values of parameters conduce to two high intensity resonance modes are provided. To ensure that the predicted data is as correct as possible, it is also recommended to choose parameter combinations that are far from transitions, and then corroborate the predicted parameters by comparison with theoretical calculations and/or micromagnetic simulations.

These results provide a simple way to find combinations of the magnetic parameters of the trilayer that have a high number of high intensity modes, thus greatly simplifying the design process of magnetic multi-band frequency devices.

Acknowledgments

AF acknowledges Universidad Mayor for covering publication fees.

ORCID iDs

A F Franco https://orcid.org/0000-0002-8366-0973

References

[1] Adam J D, Davis L E, Dionne G F, Schloemann E F and Stitzer S N 2002 *IEEE Trans. Microwave Theory Tech.* **50** 721–37
[2] Chen Y, Sakai T, Chen T, Yoon S D, Geiler A L, Vittoria C and Harris V G 2006 *Appl. Phys. Lett.* **88** 062516
[3] He P, Gao J, Marinis C T, Parimi P V, Vittoria C and Harris V G 2008 *Appl. Phys. Lett.* **93** 193505
[4] Sharma V, Khivintsev Y, Harward I, Kuanr B K and Celinski Z 2019 *J. Magn. Magn. Mater.* **489** 165412
[5] Harward I, Camley R E and Celinski Z 2014 *Appl. Phys. Lett.* **105** 173503
[6] He Y, Gao Y, Chen H, Lin H, Wei Y, Yang X and Sun N-X 2018 *IEEE Trans. Magn.* **54** 1–4
[7] Moriyama T, Finocchio G, Carpentieri M, Azzerboni B, Ralph D C and Buhrman R A 2012 *Phys. Rev.* B **86** 060411
[8] Zeng Z, Finocchio G and Jiang H 2013 *Nanoscale* **5** 2219–31
[9] Cheng R, Xiao D and Brataas A 2016 *Phys. Rev. Lett.* **116** 207603
[10] Houshang A *et al* 2018 *Nat. Commun.* **9** 4374
[11] Sluka V, Kákay A, Deac A M, Bürgler D E, Schneider C M and Hertel R 2015 *Nat. Commun.* **6** 6409
[12] Wintz S, Tiberkevich V, Weigand M, Raabe J, Lindner J, Erbe A, Slavin A and Fassbender J 2016 *Nat. Nanotechnol.* **11** 948–53
[13] Harris V G 2012 *IEEE Trans. Magn.* **48** 1075–104
[14] Falub C V, Rohrmann H, Bless M, Meduňa M, Marioni M, Schneider D, Richter J H and Padrun M 2017 *AIP Adv.* **7** 056414
[15] Mitragotri S 2013 *Adv. Drug Deliv. Rev.* **65** 100–3
[16] Yetisen A K, Martinez-Hurtado J L, Ünal B, Khademhosseini A and Butt H 2018 *Adv. Mater.* **30** 1706910
[17] Blauert J and Kiourti A 2019 *IEEE Trans. Antenn. Propag.* **67** 5054–62
[18] Cheng S and Wu Z 2011 *Adv. Funct. Mater.* **21** 2282–90
[19] Shilton R J, Travagliati M, Beltram F and Cecchini M 2014 *Adv. Mater.* **26** 4941–6
[20] Wu Z, Hjort K and Jeong S H 2015 *Proc. IEEE* **103** 1211–25
[21] Zhu W, Park S, Yogeesh M N, McNicholas K M, Bank S R and Akinwande D 2016 *Nano Lett.* **16** 2301–6 (pMID: 26977902)
[22] Li W, Torres D, Díaz R, Wang Z, Wu C, Wang C, Lin Wang Z and Sepúlveda N 2017 *Nat. Commun.* **8** 15310
[23] Xu F, Zhang D, Liao Y and Zhang H 2019 *Ceram. Int.* **45** 6350–5
[24] Vaseem M, Ghaffar F A, Farooqui M F and Shamim A 2018 *Adv. Mater. Technol.* **3** 1700242
[25] Rana B and Otani Y 2019 *Commun. Phys.* **2** 90
[26] Saadon S and Sidek O 2011 *Energy Convers. Manage.* **52** 500–4
[27] Song C, Huang Y, Zhou J, Zhang J, Yuan S and Carter P 2015 *IEEE Trans. Antenn. Propag.* **63** 3486–95
[28] Wei C and Jing X 2017 *Renew. Sustain. Energy Rev.* **74** 1–18
[29] Cheng C and Bailey W E 2013 *Appl. Phys. Lett.* **103** 242402
[30] Iakubov I T, Lagarkov A N, Osipov A V, Maklakov S A, Rozanov K N, Ryzhikov I A and Starostenko S N 2014 *AIP Adv.* **4** 107143
[31] Yu H, d' Allivy Kelly O, Cros V, Bernard R, Bortolotti P, Anane A, Brandl F, Heimbach F and Grundler D 2016 *Nat. Commun.* **7** 11255
[32] Scheunert G, Heinonen O, Hardeman R, Lapicki A, Gubbins M and Bowman R M 2016 *Appl. Phys. Rev.* **3** 011301
[33] Stenning G B G *et al* 2015 *New J. Phys.* **17** 013019
[34] Wang W, Chai G and Xue D 2017 *J. Phys. D: Appl. Phys.* **50** 365003
[35] Zuo H, Ge S, Wang Z, Xiao Y and Yao D 2010 *Scr. Mater.* **62** 766–9
[36] Chen Y, Fan X, Zhou Y, Xie Y, Wu J, Wang T, Chui S T and Xiao J Q 2015 *Adv. Mater.* **27** 1351
[37] Franco A F and Landeros P 2016 *J. Phys. D: Appl. Phys.* **49** 385003
[38] Zhao S, Gao Z, Chen C, Wang G, Zhang B, Chen Y, Zhang J, Li X and Qin Y 2016 *Carbon* **98** 196–203
[39] Guo D and Feng J 2017 *Surf. Interfaces* **9** 9–12
[40] Li S, Li Q, Xu J, Yan S, Miao G-X, Kang S, Dai Y, Jiao J and Lü Y 2016 *Adv. Funct. Mater.* **26** 3738–44
[41] Li S *et al* 2016 *Sci. Rep.* **6** 33349

[42] Franco A F 2020 *New J. Phys.* **22** 013017
[43] Carleo G, Cirac I, Cranmer K, Daudet L, Schuld M, Tishby N, Vogt-Maranto L and Zdeborová L 2019 *Rev. Mod. Phys.* **91** 045002
[44] Bohrdt A, Chiu C S, Ji G, Xu M, Greif D, Greiner M, Demler E, Grusdt F and Knap M 2019 *Nat. Phys.* **15** 921–4
[45] Liakos K, Busato P, Moshou D, Pearson S and Bochtis D 2018 *Sensors* **18** 2674
[46] Rajkomar A, Dean J and Kohane I 2019 *N. Engl. J. Med.* **380** 1347–58 (pMID: 30943338)
[47] Kitchin J R 2018 *Nat. Catal.* **1** 230–2
[48] Gusenbauer M, Oezelt H, Fischbacher J, Kovacs A, Zhao P, Woodcock T G and Schrefl T 2020 *npj Comput. Mater.* **6** 89
[49] Kwon H Y, Kim N J, Lee C K and Won C 2019 *Phys. Rev.* B **99** 024423
[50] Miao J-Y 2019 *Chin. Phys. Lett.* **36** 097501
[51] Kwon H Y, Yoon H G, Lee C, Chen G, Liu K, Schmid A K, Wu Y Z, Choi J W and Won C 2020 *Sci. Adv.* **6** eabb0872
[52] Li X-Y, Lou F, Gong X-G and Xiang H 2020 *New J. Phys.* **22** 053036
[53] Acharya U R, Oh S L, Hagiwara Y, Tan J H, Adam M, Gertych A and Tan R S 2017 *Comput. Biol. Med.* **89** 389–96
[54] Haglin J M, Jimenez G and Eltorai A E M 2019 *Health Technol.* **9** 1–6
[55] Hannun A Y, Rajpurkar P, Haghpanahi M, Tison G H, Bourn C, Turakhia M P and Ng A Y 2019 *Nat. Med.* **25** 65–9
[56] Kusumoto D and Yuasa S 2019 *Inflamm. Regen.* **39** 14
[57] Tang B, Pan Z, Yin K and Khateeb A 2019 *Front. Genet.* **10** 214
[58] Zou J, Huss M, Abid A, Mohammadi P, Torkamani A and Telenti A 2019 *Nat. Genet.* **51** 12–8
[59] Duarte J *et al* 2018 *J. Inst.* **13** P07027
[60] Goswami S, Anitescu C, Chakraborty S and Rabczuk T 2020 *Theor. Appl. Fract. Mech.* **106** 102447
[61] Choudhary A, Lindner J F, Holliday E G, Miller S T, Sinha S and Ditto W L 2020 *Phys. Rev.* E **101** 062207
[62] Cetinic E, Lipic T and Grgic S 2018 *Expert Syst. Appl.* **114** 107–18
[63] Tin M L-m 2021 Artificial neural networks in art-face colorization and 3d visualization *Intelligent Human Systems Integration 2021* ed D Russo, T Ahram, W Karwowski, G Di Bucchianico and R Taiar (Cham: Springer) pp 503–8
[64] Fabiani G and Mentink J 2019 *SciPost Phys.* **7** 4
[65] Đurić T and Ševa T 2020 *Phys. Rev.* B **102** 085104
[66] Quondam Antonio S, Riganti Fulginei F, Laudani A, Faba A and Cardelli E 2021 *J. Magn. Magn. Mater.* **528** 167735
[67] Arias R and Mills D L 1999 *Phys. Rev.* B **60** 7395–409
[68] Landeros P, Arias R E and Mills D L 2008 *Phys. Rev.* B **77** 214405
[69] Cortés-Ortuño D and Landeros P 2013 *J. Phys.: Condens. Matter* **25** 156001
[70] Newell A J, Williams W and Dunlop D J 1993 *J. Geophys. Res.* **98** 9551–5
[71] Franco A F and Landeros P 2018 *J. Phys. D: Appl. Phys.* **51** 225003
[72] Pedregosa F *et al* 2011 *Carbohydr. Res.* **346** 2825–30
[73] Bishop C 2006 *Pattern Recognition and Machine Learning* (New York: Springer)
[74] Kingma D P and Ba J 2015 Adam: a method for stochastic optimization *3rd Int. Conf. Learning Representations, ICLR 2015* (San Diego, CA, USA May 7–9, 2015) Conference Track Proceedings ed Y Bengio and Y LeCun http://arxiv.org/abs/1412.6980
[75] Chawla N V, Bowyer K W, Hall L O and Kegelmeyer W P 2002 *J. Artif. Intell. Res.* **16** 321–57
[76] Parkin S S P, More N and Roche K P 1990 *Phys. Rev. Lett.* **64** 2304–7
[77] Parkin S S P, Bhadra R and Roche K P 1991 *Phys. Rev. Lett.* **66** 2152–5
[78] Kravets A F, Polishchuk D M, Dzhezherya Y I, Tovstolytkin A I, Golub V O and Korenivski V 2016 *Phys. Rev.* B **94** 064429